Investigating transverse Hall voltages using two-terminal setups

Leandro R. F. Lima[1] and Alexis R. Hernández[2]
[1]*Instituto de Física, Universidade Federal Fluminense, 24210-346 Niterói, Brazil*
[2]*Instituto de Física, Universidade Federal do Rio de Janeiro, 21941-972 Rio de Janeiro, Brazil*

(Received 2 March 2018; revised manuscript received 12 June 2018; published 4 September 2018)

In this paper, we present a method to numerically study transverse Hall voltages using an alternative quantity in two-terminal setups. Using nonlinear transport concepts, we find that the Hall voltage dependence on the model parameters can be investigated from the difference between the injectivities of each terminal. The method is suitable to work with nonequilibrium Green's functions as well as for scattering matrix approaches. We illustrate the proposed idea by studying the quantum spin Hall effect in graphene with disordered spin-orbit scattering centers induced by adatoms. We use two distinct models: a finite-difference implementation of the Dirac Hamiltonian and a tight-binding Hamiltonian combined with the scattering matrix approach and the nonequilibrium Green's functions approach, respectively.

DOI: 10.1103/PhysRevB.98.115404

I. INTRODUCTION

The bloom of topological ideas in the condensed-matter community is one of the driving forces propelling new discoveries in the field. The most prominent topological effect of quantum matter is the quantum Hall effect (QHE) [1,2], in which a strong magnetic field, perpendicular to the sample, leads to an electronic current that flows only through the sample edges and it is robust against backscattering.

In the past two decades, another topological effect, called the quantum spin Hall effect (QSHE) [1], was theoretically predicted [3] and experimentally confirmed [4]. Here spin-orbit coupling (SOC) gives rise to spin-polarized charge propagation through opposite edges of the sample [1]. The QSHE has been in the spotlight ever since its observation in HgTe/CdTe quantum wells [4]. The latter triggered an intense investigation of the robustness of spin-polarized current against nonmagnetic disorder and how it is affected by time-reversal symmetry breaking caused by an external magnetic field [5–8].

There are other topological states associated with edge/surface current propagation in condensed-matter physics, such as the states in the quantum anomalous Hall effect, in chiral topological superconductors, and in Weyl semimetals [1]. The protagonist in almost any case are the chiral states that arise as a consequence of nontrivial topologies. To address these states, experimentalists usually need samples with four- or six-terminal geometries to measure the transverse charge or spin conductances. However, the theoretical study of such systems with realistic sizes and disorder demands the use of numerical methods, such as the recursive Green's-function method [9,10]. Although methods to treat the electronic transport in multiterminal setups have been developed over the years [11–15], the use of multiple terminals undermines the size and speed capabilities of the method as compared to a simple two-terminal setup.

In this paper, we describe how to overcome this shortcoming by alternatively using two-terminal calculations to study the dependence of transverse voltage differences on model parameters. To illustrate the method, we address the QSHE in graphene doped with adatoms [16,17] using two different methods: A finite-difference method, which computes the scattering matrix for Dirac particles [18] in a strip geometry, and the usual tight-binding description [19] combined with nonequilibrium Green's functions.

The paper is organized as follows: Section II introduces the general ideas from nonlinear transport that are relevant to this study. Next we describe how to study transverse conductances using those concepts in Sec. III. We devote Sec. IV to an illustration of the method by investigating the spin accumulation at the edges of graphene nanoribbons due to the presence of disordered spin-orbit scattering centers. We conclude in Sec. V.

II. NONLINEAR TRANSPORT

The Landauer-Büttiker formula is a cornerstone in the study of electronic transport in mesoscopic systems. It allows for the computation of the electronic current, at a particular contact, in terms of the electronic transmission probabilities. Following the notation of Ref. [20], the Landauer-Büttiker formula for the electronic current at terminal α reads

$$I_\alpha = \frac{2e}{h}\sum_{\beta=1}^{N}\int_{-\infty}^{\infty} dE\, f_\beta(E)\, A_{\alpha\beta}[E, U(\mathbf{r})], \tag{1}$$

where $f_\beta(E) = f_0(E - eV_\beta)$, V_β represents the electronic distribution function and the electrostatic potential at the contact β, respectively, and $f_0(E) = [e^{(E-E_F)/k_BT} + 1]^{-1}$ is the equilibrium Fermi-Dirac distribution function at temperature T and Fermi energy E_F. The factor 2 accounts for the spin degeneracy. The quantity $A_{\alpha\beta}[E, U(\mathbf{r})]$, which encodes the transmission properties of the system, is expressed in terms of the scattering matrix $\mathbf{S}_{\alpha\beta}$ as

$$A_{\alpha\beta}[E, U(\mathbf{r})] = \mathrm{Tr}[\mathbf{1}_\alpha\delta_{\alpha\beta} - \mathbf{S}^\dagger_{\alpha\beta}\mathbf{S}_{\alpha\beta}]. \tag{2}$$

In Eqs. (1) and (2), we make explicit the dependence of the transmission amplitudes on the electrostatic potential $U(\mathbf{r}) = U(\mathbf{r}, \{V_\alpha\})$ inside the system. In linear response, $A_{\alpha\beta}$

is computed at the equilibrium potential $U_{\rm eq}(\mathbf{r})$ which is established when all reservoirs have the same equilibrium chemical potential μ_0. Beyond this regime, it is necessary to compute $U(\mathbf{r})$ self-consistently, as pointed out by Landauer [21].

To make analytical progress, it is convenient to expand all quantities in powers of V_α. The local electrostatic potential $U(\mathbf{r})$ reads

$$U(\mathbf{r}) = U_{\rm eq}(\mathbf{r}) + \sum_\alpha u_\alpha(\mathbf{r}) V_\alpha + O(V_\alpha^2), \tag{3}$$

where $u_\alpha(\mathbf{r})$ is the characteristic potential defined by

$$u_\alpha(\mathbf{r}) = \frac{\partial}{\partial V_\alpha} U(\mathbf{r})\bigg|_{\{V_\gamma\}=0}. \tag{4}$$

Here $\{V_\gamma\} = 0$ is a shorthand for $V_\gamma = 0$ for all γ.

To determine $u_\alpha(\mathbf{r})$, we need a self-consistent microscopic electronic structure calculation, or we find an adequate approximation for it. The latter was developed in Ref. [22] assuming that the potential $U(\mathbf{r})$ is related to the electronic density imbalance $\delta n(\mathbf{r})$ generated by the bias. In turn, $\delta n(\mathbf{r})$ arises from the charge injected by the leads $\delta n_{\rm inj}(\mathbf{r})$ and the correspondent-induced charge in the conductor $\delta n_{\rm ind}(\mathbf{r})$.

At linear order, the injected charge $\delta n_{\rm inj}(\mathbf{r})$ is proportional to the injection properties of the sample which is given by the injectivity, namely

$$\frac{dn(\mathbf{r},\alpha)}{dE} = -\frac{1}{2\pi i}\int_{-\infty}^{\infty} dE\left(-\frac{\partial f_0}{\partial E}\right) \times \sum_\beta {\rm Tr}\left[\mathbf{S}^\dagger_{\beta\alpha}\frac{\delta \mathbf{S}_{\beta\alpha}}{e\delta U(\mathbf{r})} - \frac{\delta \mathbf{S}^\dagger_{\beta\alpha}}{e\delta U(\mathbf{r})}\mathbf{S}_{\beta\alpha}\right], \tag{5}$$

evaluated at $\{V_\gamma\} = 0$. Here we included the factor 2 due to spin degeneracy. The injectivity describes the linear contribution to the local density of states related to incoming states from a given contact.

The induced electronic density, up to linear order in V, is given by $\delta n_{\rm ind}(\mathbf{r}) = \sum_\alpha \frac{dn^\alpha_{\rm ind}(\mathbf{r})}{dE} eV_\alpha$, where

$$\frac{dn^\alpha_{\rm ind}(\mathbf{r})}{dE} = \int d\mathbf{r}'\, \Pi(\mathbf{r},\mathbf{r}')\, u_\alpha(\mathbf{r}') \tag{6}$$

and $\Pi(\mathbf{r},\mathbf{r}')$ is the Lindhard polarization function [20,23].

These elements render the Poisson equation

$$-\nabla^2 u_\alpha(\mathbf{r}) + 4\pi e^2 \frac{dn^\alpha_{\rm ind}(\mathbf{r})}{dE} = 4\pi e^2 \frac{dn(\mathbf{r},\alpha)}{dE}, \tag{7}$$

where the injected charge $e^2 dn(\mathbf{r},\alpha)/dE$ depends only on the scattering matrix and $e^2 dn^\alpha_{\rm ind}(\mathbf{r})/dE$ is the charge induced by the injected one.

The scattering approach does not provide a recipe to obtain $\Pi(\mathbf{r},\mathbf{r}')$. An usual procedure is to take advantage of the Thomas-Fermi approximation [20,22] where the induced charge density is proportional to the local density of states $\frac{dn(\mathbf{r})}{dE}$, namely

$$\frac{dn^\alpha_{\rm ind}(\mathbf{r})}{dE} = \frac{dn(\mathbf{r})}{dE} u_\alpha(\mathbf{r}). \tag{8}$$

However, the Thomas-Fermi approximation may underestimate the screening capabilities of the system when the local chemical potential lies at a vanishing density of states point such as the Dirac point in bulk graphene [24]. In what follows, we describe a procedure that allows us to study the Hall voltage dependence on model parameters without knowing the details of the screening contribution.

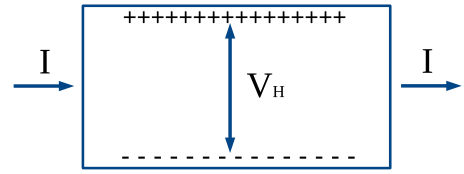

FIG. 1. Schematic view of the system. The electronic current I enters through terminal 1 (left) and leaves through terminal 2 (right). The upper (lower) edge is positively (negatively) charged giving rise to a Hall voltage V_H. The magnetic field is perpendicular to the system.

III. CHARGE AND SPIN HALL VOLTAGES

In the presence of a perpendicular magnetic field, the current I passing through the system illustrated in Fig. 1 generates a Hall voltage V_H established in the transverse direction due to charge accumulation at the edges. The Hall conductance in such a system is defined as

$$\sigma_H = \frac{I}{V_H}. \tag{9}$$

For a two-terminal system such as the one in Fig. 1, the electronic current I is given by the Landauer formula in Eq. (1). For a small bias, we evaluate I at $U_{\rm eq}(\mathbf{r})$ and compute the Hall voltage V_H in terms of the characteristic potentials u_α by means of Eq. (3). In linear response, V_H reads

$$\begin{aligned} V_H(x) &= U(\mathbf{r}_+) - U(\mathbf{r}_-), \\ &= [u_1(\mathbf{r}_+)V_1 + u_2(\mathbf{r}_+)V_2] - [u_1(\mathbf{r}_-)V_1 + u_2(\mathbf{r}_-)V_2], \end{aligned} \tag{10}$$

where $\mathbf{r}_+ = (x, y_+)$ and $\mathbf{r}_- = (x, y_-)$ correspond to the edges of the system at the same longitudinal coordinate x. For a symmetric applied voltage, i.e., $V_1 = -V_2 = V/2$, we find

$$V_H(x) = [\Delta u(\mathbf{r}_+) - \Delta u(\mathbf{r}_-)]V/2, \tag{11}$$

where $\Delta u(\mathbf{r}) \equiv u_1(\mathbf{r}) - u_2(\mathbf{r})$.

The Hall voltage V_H in Eq. (11) depends on the two-terminal characteristic potential difference $\Delta u(\mathrm{r})$ instead of the individual values u_α. From Eq. (7) we find that $\Delta u(\mathbf{r})$ is given by

$$-\nabla^2 \Delta u(\mathbf{r}) + 4\pi e^2 \Delta n_{\rm ind}(\mathbf{r}) = 4\pi e^2 \Delta n(\mathbf{r}), \tag{12}$$

where $\Delta n(\mathbf{r}) \equiv \frac{dn(\mathbf{r},1)}{dE} - \frac{dn(\mathbf{r},2)}{dE}$ is the two-terminal injectivity difference at the position $\mathbf{r}$, and $\Delta n_{\rm ind}(\mathbf{r})$ is the screening density induced by $\Delta n(\mathbf{r})$.

The characteristic potential $\Delta u(\mathbf{r})$ increases monotonically with the charge accumulated at the region $\Omega_\mathbf{r}$ surrounding $\mathbf{r}$. The accumulated charge is the result of the difference between the injected and the screening charges. Since the screening contribution cannot exceed the injected contribution, this ensures that an increase in the injected charge in a particular region $\Omega_\mathbf{r}$ leads to an increase in the electrostatic potential at $\mathbf{r}$. In the case of a symmetric bias voltage, the injected

charge is given by $q_{\rm inj}(\mathbf{r}) \propto e^2 V \Delta n(\mathbf{r})$ [20]. This ensures that $\Delta u(\mathbf{r})$ monotonically increases with Δn accumulated at $\Omega_{\mathbf{r}}$. Therefore, we can study the behavior of the Hall voltage, which is proportional to $\Delta u(\mathbf{r}_+) - \Delta u(\mathbf{r}_-)$, throughout the injectivity imbalance Δn.

Although the analytical dependence of the Hall voltage V_H in Eq. (11) on Δn is unknown, it is possible to study the injection density Δn, or its imbalance $\Delta_\pm(x)$ defined as the difference between Δn accumulated in $\Omega_{\mathbf{r}_+}$ and $\Omega_{\mathbf{r}_-}$, in order to determine (i) whether the QHE is present ($\Delta_\pm \neq 0 \Rightarrow V_H \neq 0$) or not ($\Delta_\pm = 0 \Rightarrow V_H = 0$) and (ii) if the QHE becomes stronger or weaker by varying any model parameter, since V_H varies monotonically with $\Delta_\pm$.

Spin-dependent effects, such as the QSHE, cannot be directly quantified by the characteristic potentials in Eq. (7) because they do not distinguish the spin degrees of freedom. On the other hand, one can calculate the spin-resolved injectivities $\frac{dn^s(\mathbf{r},\alpha)}{dE}$, where $s = \uparrow, \downarrow$ labels the spin, to obtain the two-terminal spin-resolved injection densities

$$\Delta n^s(\mathbf{r}) = \left(\frac{dn^s(\mathbf{r},1)}{dE} - \frac{dn^s(\mathbf{r},2)}{dE} \right). \tag{13}$$

Thus, it is straightforward to extend the ideas discussed for the Hall voltage V_H to study the spin Hall voltage $V_{\rm SH}$ by studying the imbalance $\Delta^s_\pm(x)$, defined as the difference between Δn^s in Eq. (13) accumulated in $\Omega_{\mathbf{r}_+}$ and $\Omega_{\mathbf{r}_-}$. In this case, the spin-resolved imbalance $\Delta^s_\pm(x)$ generates the spin-Hall voltage $V^s_{\rm SH}(x)$ for the spin orientation $s = \uparrow, \downarrow$.

In the next sections, we use Eq. (13) to quantitatively analyze the dependence of the QSHE in graphene nanoribbons doped with spin-orbit scatterers on a few model parameters.

IV. QUANTUM SPIN HALL EFFECT: GRAPHENE NANORIBBONS WITH DISORDERED SPIN-ORBIT COUPLING

We study local disordered spin-orbit coupling on graphene due to the presence of adatoms deposited on top of the graphene sheet. This system has been shown to present the QSHE both theoretically [16,19] and experimentally [17]. First we study numerically the density of spin accumulation for a finite-size graphene nanoribbon doped with adatoms using the scattering matrix approach applied to the effective low-energy continuous description given by the Dirac Hamiltonian. Then we analyze the same system described by a full tight-binding Hamiltonian for graphene with effective local hoppings that mimic the presence of adatoms.

A. Scattering matrix approach

In this section, we use the finite-difference method presented in Ref. [18] to compute the scattering matrix of massless Dirac particles with spin-orbit coupling disorder. The Hamiltonian is

$$H = -i\hbar v(\sigma_x \partial_x + \sigma_y \partial_y) + U^{\rm ad}_{\rm nm}(\mathbf{r}) + U^{\rm ad}_{\rm m}(\mathbf{r}), \tag{14}$$

where v is the velocity of the massless Dirac fermions, σ_x and σ_y are Pauli matrices associated with the pseudospin (sublattices), $U^{\rm ad}_{\rm nm}(\mathbf{r})$ is an electrostatic potential due to nonmagnetic adatoms, and $U^{\rm ad}_{\rm m}(\mathbf{r})$ is the spin-orbit term that appears due to the presence of magnetic adatoms. Magnetic and nonmagnetic adatoms are randomly distributed in the system with concentrations $n_{\rm SOC}$ and $n_{\rm dis}$, respectively. The nonmagnetic contribution to the potential is given by $U^{\rm ad}_{\rm nm}(\mathbf{r}) = \sum_j U_{\rm dis}\delta(\mathbf{r} - \bar{\mathbf{r}}_j)$, where $U_{\rm dis}$ is the impurity disorder strength and $\bar{\mathbf{r}}_\mathbf{j}$ indicates the nonmagnetic adatoms positions. The presence of magnetic adatoms generates a local spin-orbit interaction and a local change in the electrostatic potential as well. The potential due to magnetic adatoms is $U^{\rm ad}_{\rm m}(\mathbf{r}) = \sum_j [U_{\rm SOC}\sigma_z \otimes \tau_z \delta(\mathbf{r} - \tilde{\mathbf{r}}_j) + U_C \delta(\mathbf{r} - \tilde{\mathbf{r}}_j)]$, where $U_{\rm SOC}$ is the spin-orbit strength, U_C is the magnetic adatom disorder strength, $\tilde{\mathbf{r}}_j$ indicates the position where magnetic adatoms are located, and the Pauli matrices τ_z refer to the spin degree of freedom.

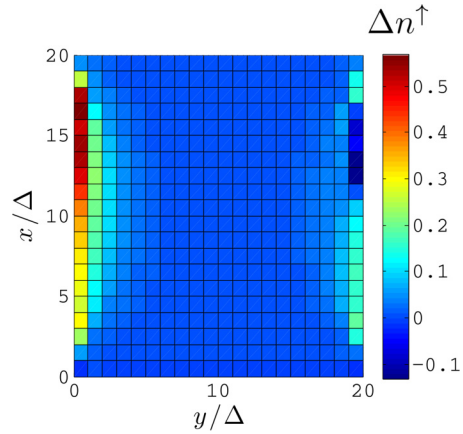

FIG. 2. Injection density of spin-up electrons $\Delta n^\uparrow$ in units of $1/(\text{nm})^2\text{eV}$ for a single realization. The system has width $W = 20\Delta$ and length $L = 20\Delta$, where $\Delta = 0.71$ nm. The disorder concentration is 5%, the SOC disorder strength is $U_{\rm SOC} = 0.02$ eV, and the electronic energy is $E = -0.001$ eV. The transport occurs in the x direction.

To study the QSHE, we need to compute the injectivities for this system. To do that, we numerically calculate the functional derivative of the scattering matrix as

$$\frac{\delta \mathbf{S}_{\alpha\beta}}{\delta U(\mathbf{r}_0)} = \lim_{\xi \to 0} \frac{\mathbf{S}_{\alpha\beta}[U(\mathbf{r}) + \xi\delta(\mathbf{r} - \mathbf{r}_0)] - \mathbf{S}_{\alpha\beta}[U(\mathbf{r})]}{\xi}, \tag{15}$$

we substitute the result in Eq. (5), and we evaluate the injectivities at zero temperature. We discretize the system using the lattice spacing $\Delta = 0.71$ nm. The nanoribbon has width $W = 20\Delta$ and length $L = 20\Delta$; see Fig. 2. The system is attached to vertical semi-infinite leads at the positions $x = 0$ and $x = L$.

Figure 2 shows a single realization of the spin-up injection density $\Delta n^\uparrow$ in units of $1/(\text{nm})^2\text{eV}$ for a symmetric bias. The disorder concentration is $n_c = 5\%$ and the SO disorder strength is $U_{\rm SOC} = 0.02$ eV. The injection properties are calculated at electronic energy $E = -0.001$ eV. We find a clear and strong spin-up imbalance $\Delta^\uparrow_\pm = \Delta n^\uparrow(y = 0) - \Delta n^\uparrow(y = W) > 0$ between the opposite edges of the system. Due to the symmetries of the SO interaction, the spin-down injection density $\Delta n^\downarrow$ (not shown here) produces the same absolute imbalance but with opposite sign $\Delta^\downarrow_\pm = -\Delta^\uparrow_\pm$. The results indicate that the QSHE is indeed present with opposite spin Hall voltages $V^\downarrow_{\rm SH} = -V^\uparrow_{\rm SH}$.

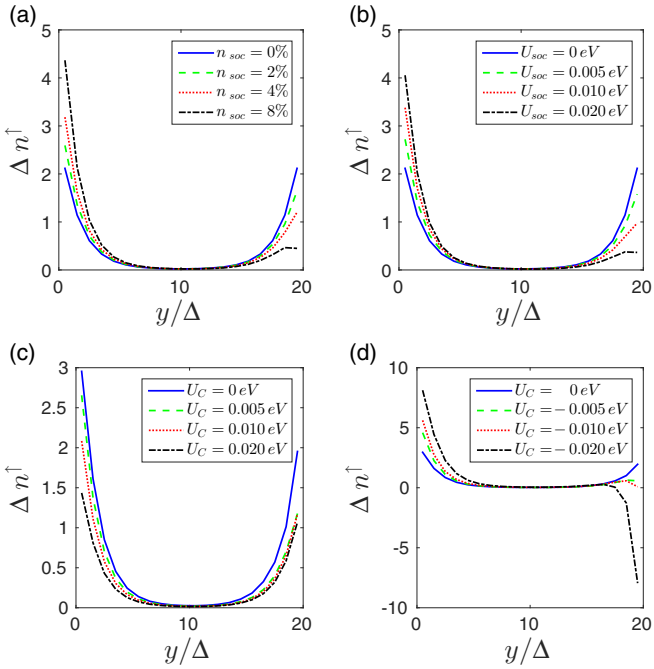

FIG. 3. Spin-up injection density $\Delta n^{\uparrow}$ in units of $1/(\text{nm})^2\text{eV}$ calculated at $x = L/2$ as a function of the transverse coordinate y across the ribbon width. The results correspond to an average over 1000 realizations, where we set $E = -0.001$ eV, $L = 20\Delta$, $W = 20\Delta$, and $\Delta = 0.71$ nm. In panel (a) we use $U_C = 0$, $U_{\text{dis}} = 0$, $U_{\text{SOC}} = 0.01$ eV, and vary the SOC disorder concentration n_{SOC}. In (b) we vary the SOC strength U_{SOC} by keeping the concentration constant $n_{\text{SOC}} = 5\%$. We turn on the SOC Coulomb contribution U_C in panels (c) and (d). The SOC strength is $U_{\text{SOC}} = 0.01$ eV and the concentration is $n_{\text{SOC}} = 5\%$. In (c) the Coulomb potential assumes positive values while assuming negative values in (d).

To study the dependence of the QSHE on the model parameters, we plot the average over disorder configurations of the transverse section of the spin-up injection density $\Delta n^{\uparrow}$ across the width in Fig. 3. First we turn off the local Coulomb potential $U_C = 0$ and the disorder potential $U_{\text{dis}} = 0$. We vary the concentration n_C in Fig. 3(a) using a local spin-orbit coupling $U_{\text{SOC}} = 0.01$ eV. In the absence of adatoms $n_c = 0$ there is no injection imbalance ($\Delta^{\uparrow}_{\pm} = 0$). As we increase the concentration up to $n_c = 8\%$, the injection imbalance $\Delta^{\uparrow}_{\pm}$ increases as well showing a monotonic increase in the interval $n_c \in [0, 8\%]$. Figure 3(b) shows the dependence of $\Delta n^{\uparrow}$ on the local spin-orbit coupling U_{SOC} for $U_C = 0$ and $n_c = 5\%$. We find that the injection imbalance also increases monotonically with the local spin-orbit strength U_{SOC}.

In Figs. 3(c) and 3(d) we keep U_{SOC} and n_C constant, turning on the local Coulomb potential to analyze the dependence of $\Delta n^{\uparrow}$ on U_C. Figure 3(c) shows that by increasing U_C, the injection imbalance $\Delta^{\uparrow}_{\pm}$ decreases for positive values of U_C. The injection density $\Delta n^{\uparrow}(y = W)$ remains roughly constant while $\Delta n^{\uparrow}(y = 0)$ decreases in the interval $[0.005, 0.020]$ eV, decreasing $\Delta^{\uparrow}_{\pm}$ as a consequence. On the other hand, Fig. 3(d) shows the opposite behavior for negative values of U_C. As U_C varies from $U_C = 0$ to $U_C = -0.020$ eV, the imbalance $\Delta^{\uparrow}_{\pm}$ increases. Thus, spin-up Hall voltage $V^{\uparrow}_{\text{SH}}$ decreases with $|U_C|$ for positively charged adatoms and increases with $|U_C|$ for negatively charged adatoms.

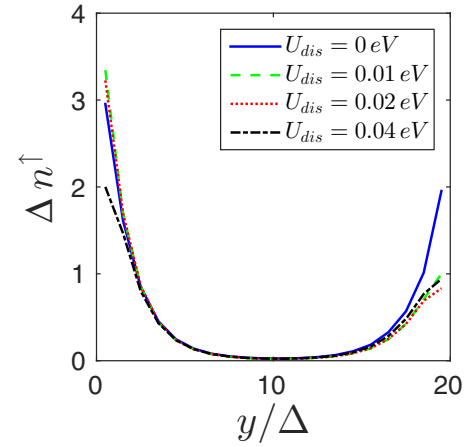

FIG. 4. Spin-up injection density $\Delta n^{\uparrow}$ in units of $1/(\text{nm})^2\text{eV}$ calculated at $x = L/2$ as a function of the transverse coordinate y across the ribbon width. The results correspond to an average over 1000 realizations, where we set $E_F = -0.001$ eV, $L = 20\Delta$, $W = 20\Delta$, and $\Delta = 0.71$ nm. We use $U_{\text{SOC}} = 0.01$ eV, $U_C = 0$, $n_{\text{SOC}} = 5\%$, $n_{\text{dis}} = 5\%$, and vary the nonmagnetic disorder strength U_{dis} from 0 to 0.04 eV. See the main text for more details.

Next we consider the diagonal disorder produced by a different source $U_{\text{dis}}(\mathbf{r})$. These additional scatterers are nonmagnetic and are placed in positions that are different from the adatoms positions. In this case, the system has a coverage $n_{\text{SOC}} = 5\%$ of adatoms with SOC $U_{\text{SOC}} = 0.01$ eV and Coulomb strength $U_C = 0$. Figure 4 shows the spin-up injection density $\Delta n^{\uparrow}$ as a function of the nonmagnetic disorder strength U_{dis} for a nonmagnetic disorder coverage $n_{\text{dis}} = 5\%$. The plot shows that $\Delta n^{\uparrow}$ does not vary monotonically with the disorder strength U_{dis}. The injection imbalance between the edges $\Delta^{\uparrow}_{\pm}$ increases when U_{dis} varies from 0 to 0.01 eV and decreases when U_{dis} varies from 0.01 to 0.04 eV. As a matter of fact, there is an optimal value of the disorder strength, which is roughly $U_{\text{dis}} = 0.01$ eV, that maximizes the injection imbalance $\Delta^{\uparrow}_{\pm}$ between opposite edges and the spin Hall voltages V^{s}_{SH} as a consequence.

B. Green's-function approach applied to the quantum spin Hall effect on graphene

In this section, we present our numerical results on the spin-resolved injection density Δn^{s} for a finite-size graphene nanoribbon doped with adatoms using the tight-binding model proposed in Ref. [16]. Within this model, we also expect an imbalance $\Delta^{s}_{\pm} \neq 0$ in the spin-resolved injection density due to the QSHE generated by the presence of adatoms that act as spin-orbit scattering centers for electronic energies near the charge-neutrality point.

The tight-binding description of graphene including the contribution from the adatoms reads [16,25–27]

$$H = -t \sum_{\langle i,j\rangle,\sigma} c^{\dagger}_{i\sigma} c_{j\sigma} + \sum_{j,\sigma} \epsilon_j c^{\dagger}_{j\sigma} c_{j\sigma} + i t_{\text{SO}} \sum_{\langle\langle i,j\rangle\rangle,\sigma\sigma'} v_{ij} c^{\dagger}_{i\sigma} \tau^{z}_{\sigma\sigma'} c_{j\sigma'}. \quad (16)$$

The operator $c^{\dagger}_{i\sigma}$ ($c_{j\sigma}$) creates (destroys) an electron with spin $\sigma = \uparrow, \downarrow$ at the site i (j). The hopping integral between first neighbors in the kinetic term has a value $t = 2.7$ eV, and ϵ_j are on-site energies randomly chosen from a uniform distribution in the interval $[-V_{\rm dis}, V_{\rm dis}]$, where $V_{\rm dis}$ is the disorder strength. The spin-orbit interaction due to adatoms in the third term has strength $t_{\rm SO}$ and acts only between second neighbors around the adatom, which is placed at the center of the corresponding hexagon. Here the magnetic adatoms are randomly distributed in the system with a concentration $n_{\rm AD}$, while the presence of nonmagnetic adatoms is modeled by the random on-site energies ϵ_j described above. The Pauli matrix τ^z ensures that the hopping has opposite signs for different spin orientations while ν_{ij} distinguishes between the clockwise ($\nu_{ij} = 1$) and the counterclockwise ($\nu_{ij} = -1$) directions [16]. For simplicity, we study the electronic transport properties neglecting the Rashba coupling [28].

One of the most efficient ways to calculate transport properties of two-terminal systems is the Green's-functions technique [29,30]. We calculate the nonequilibrium injectivity in Eq. (5) in terms of equilibrium Green's functions as [20]

$$\left.\frac{dn(j,\alpha)}{dE}\right|_{E=E_F} = \int_{-\infty}^{\infty} \frac{dE}{2\pi}\left(-\frac{\partial f_0}{\partial E}\right)\langle j|G_0^r \Gamma_\alpha G_0^a|j\rangle, \quad (17)$$

where G_0^r (G_0^a) is the equilibrium retarded (advanced) Green's function and Γ_α is the linewidth function of the lead α. We calculate G_0^r and Γ_α at a given electronic energy E by means of the recursive Green's-function technique (RGF) [9,10,14] and decimation [10,31], respectively. We compute the advanced Green's function via its standard relation with the retarded one, namely $G_0^a = (G_0^r)^{\dagger}$. At zero temperature, the injectivity in Eq. (17) yields

$$\left.\frac{dn^s(j,\alpha)}{dE}\right|_{E=E_F} = \frac{1}{2\pi}\langle j|G_0^{r,ss}\Gamma_\alpha^{ss} G_0^{a,ss}|j\rangle, \quad (18)$$

where E_F is the Fermi energy at equilibrium, and $G_0^{r,ss}$ ($G_0^{a,ss}$) is the equilibrium retarded (advanced) Green's-function block connecting the same spin orientation $s = \uparrow, \downarrow$. We assume that up and down spin components are equally injected in the system, $\Gamma_\alpha^{\downarrow\downarrow} = \Gamma_\alpha^{\uparrow\uparrow}$. Our model system is a graphene nanoribbon with armchair edges along the transport direction with width and length equal to 100 and 170 Å, respectively. We attach two semi-infinite armchair graphene nanoribbons as leads at $x = 0$ (left) and $x = 170$ Å (right).

Figure 5 shows the numerical results obtained by means of the spin-up component of Eq. (18). We show the spin-up injection density $\Delta n^{\uparrow}$ for a single realization as the color map in Fig. 5(a). Analogously to the previous section, we find that $\Delta n^{\uparrow}$ is higher at one edge ($y = 0$) than at the opposite one ($y = 100$ Å). The maximum and minimum values of $\Delta n^{\uparrow}$ at each cross section along the y direction, indicated by the dashed line in Fig. 5(a), are different due to the presence of the disordered distribution of adatoms in the system.

The oscillations in Fig. 5 are reminiscent of the clean armchair graphene nanoribbon structure. For each particular ribbon width there is a correspondent wave-function nodal structure in the lattice. This can be seen by solving the analytical problem using boundary conditions where the wave function vanishes at the ribbon edges. As a consequence, bonds connecting carbon sites at wave-function nodes cannot contribute to the transport by carrying electronic current [32–34].

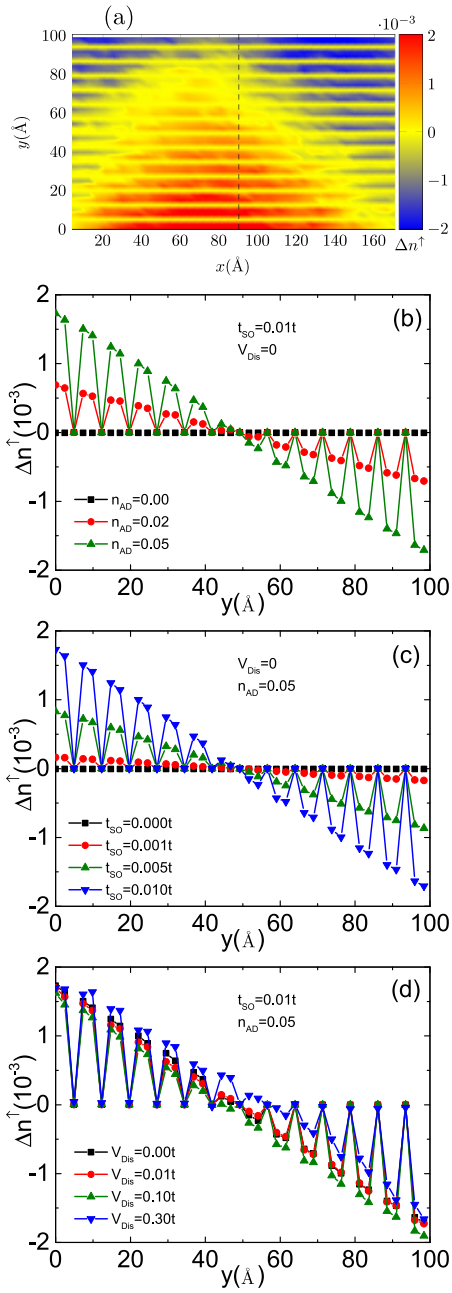

FIG. 5. (a) Spin-up injection density $\Delta n^{\uparrow}$ in units of 1/eV in a 100 Å × 170 Å graphene nanoribbon for a single realization, where $n_{\rm AD} = 0.05$, $t_{\rm SO} = 0.01t$, and $V_{\rm dis} = 0$. The dashed line indicates one of the cross sections used to calculate the average over all the cross sections that we show in panels (b)–(d) as a function of y. Panels (b), (c), and (d) show the average value of $\Delta n^{\uparrow}$ for different values of adatom concentration $n_{\rm AD}$, spin-orbit strength $t_{\rm SO}$, and disorder strength W, respectively. The electronic energy is $E_F = 0.01t$ in all results.

Panels (b), (c), and (d) of Fig. 5 show the average injection densities $\Delta n^{\uparrow}$ taken over all the cross sections in the system for different values of the adatom concentration n_{AD}, the spin-orbit strength t_{SO}, and the disorder strength V_{dis}, respectively. From Fig. 5(b) we find that $\Delta n^{\uparrow}$ vanishes in the absence of adatoms $n_{\mathrm{AD}} = 0$ (no spin orbit) and increases at the edges as we increase the adatom concentration n_{AD}. The effect is most prominent at the edges, and $\Delta n^{\uparrow}$ varies almost linearly from one edge to the opposite one.

We find a similar behavior in Fig. 5(c) where $\Delta n^{\uparrow}$ vanishes in the absence of the spin-orbit strength ($t_{\mathrm{SO}} = 0$) and increases with its value having an approximately linear dependence with y. In Fig. 5(d) we show that these results are robust against disorder. As we increase the disorder strength V_{dis} we find only small fluctuations in $\Delta n^{\uparrow}$ compared to the case without diagonal nonmagnetic disorder ($V_{\mathrm{dis}} = 0$). We find that the injection density imbalance $\Delta_{\pm}^{\uparrow}$ increases with both the adatom concentration and the spin-orbit strength t_{SO}, similarly to the results of the previous section. On the other hand, the nonmagnetic disorder within this model barely affects the imbalance $\Delta_{\pm}^{\uparrow}$, which is at odds with the previous section results. Therefore, the spin Hall voltage $V_{\mathrm{SH}}^{\uparrow}$ increases with both the adatom concentration and the spin-orbit strength t_{SO}, and it is robust against nonmagnetic disorder.

Our results are in line with the full conductance calculations performed in Ref. [16] in the absence of Rashba spin-orbit coupling. By studying the injectivities, we find that the topological phase is robust to strong fluctuations of uncorrelated nonmagnetic on-site disorder, as shown by the marginal degrading of the injectivity in Fig. 5(d). Moreover, we find that the spin-Hall voltage increases with both the magnetic adatom concentration n_{AD} and the spin-orbit strength t_{SOC}. By increasing the number of scattering centers and/or the spin-orbit intensity, we increase the asymmetric scattering for different spin orientations and enhance the spin Hall effect in the system. This effect is closely related to the increasing of the spin-orbit gap with n_{AD} and t_{SOC} in the bulk band-structure calculations in Ref. [16].

V. CONCLUSIONS

We presented a method to numerically study transverse conductances using a two-terminal setup. We established a connection between the transverse voltage in the system and the differences between the injectivities from each terminal. The connection is derived using nonlinear transport concepts from the literature.

We applied our method to study the QSHE in graphene doped with adatoms within two distinct models: a finite-difference implementation of the Dirac Hamiltonian combined with the scattering matrix approach, and a tight-binding Hamiltonian combined with the nonequilibrium Green's-functions approach. The results show that the presence of adatoms produces a considerable difference between the spin injection densities at the edges of the ribbon, resulting in a QSHE, i.e., leading to nonzero spin Hall voltages $V_{\mathrm{SH}}^{\uparrow,\downarrow}$. The latter increases with the adatom concentration and the SOC strength for both models, which is in agreement with the expected behavior of the QSHE in graphene doped with adatoms for electronic energies near the charge-neutrality point [16,25].

In the model using the tight-binding description of graphene, we found that nonmagnetic disorder does not affect the spin Hall voltages. On the other hand, in the continuum description using the Dirac Hamiltonian, the nonmagnetic disorder can increase or decrease the spin Hall voltages depending on both the intensity and the sign of the disorder strength. Furthermore, we find the optimal value of the nonmagnetic disorder strength that maximizes the spin Hall voltages. These results show that it is indeed possible to extract not only qualitative but also quantitative information on the system by studying the two-terminal injectivities using the proposed method.

ACKNOWLEDGMENTS

We thank Dr. R. B. Muniz and Dr. A. Latgé for useful suggestions to the manuscript. L.R.F.L. acknowledges the financial support of the Brazilian funding agency FAPERJ (Grant No. E-26/202.768/2016).

[1] J. Wang and S.-C. Zhang, Nat. Mater. **16**, 1062 (2017).
[2] K. v. Klitzing, G. Dorda, and M. Pepper, Phys. Rev. Lett. **45**, 494 (1980).
[3] B. A. Bernevig, T. L. Hughes, and S.-C. Zhang, Science **314**, 1757 (2006).
[4] M. König, S. Wiedmann, C. Brüne, A. Roth, H. Buhmann, L. W. Molenkamp, X.-L. Qi, and S.-C. Zhang, Science **318**, 766 (2007).
[5] J. Maciejko, X.-L. Qi, and S.-C. Zhang, Phys. Rev. B **82**, 155310 (2010).
[6] B. Scharf, A. Matos-Abiague, and J. Fabian, Phys. Rev. B **86**, 075418 (2012).
[7] M. V. Durnev and S. A. Tarasenko, Phys. Rev. B **93**, 075434 (2016).
[8] D. Nanclares, L. R. F. Lima, C. H. Lewenkopf, and L. G. G. V. D. da Silva, Phys. Rev. B **96**, 155302 (2017).
[9] A. MacKinnon, Z. Phys. B **59**, 385 (1985).
[10] C. Lewenkopf and E. Mucciolo, J. Comput. Electron. **12**, 203 (2013).
[11] H. U. Baranger, A. D. Stone, and D. P. DiVincenzo, Phys. Rev. B **37**, 6521 (1988).
[12] K. Kazymyrenko and X. Waintal, Phys. Rev. B **77**, 115119 (2008).
[13] G. Thorgilsson, G. Viktorsson, and S. Erlingsson, J. Comp. Phys. **261**, 256 (2014).
[14] L. R. F. Lima, A. Dusko, and C. Lewenkopf, Phys. Rev. B **97**, 165405 (2018).
[15] T. C. Vasconcelos, J. G. G. S. Ramos, and A. L. R. Barbosa, Phys. Rev. B **93**, 115120 (2016).
[16] C. Weeks, J. Hu, J. Alicea, M. Franz, and R. Wu, Phys. Rev. X **1**, 021001 (2011).
[17] J. Balakrishnan, G. Koon, A. Avsar, Y. Ho, J. Lee, M. Jaiswal, S.-J. Baeck, J.-H. Ahn, A. Ferreira, M. Cazalilla, A. Castro Neto, and B. Özyilmaz, Nat. Commun. **5**, 4748 (2014).

[18] A. R. Hernández and C. H. Lewenkopf, Phys. Rev. B **86**, 155439 (2012).
[19] A. H. Castro Neto and F. Guinea, Phys. Rev. Lett. **103**, 026804 (2009).
[20] A. R. Hernández and C. H. Lewenkopf, Eur. Phys. J. B **86**, 131 (2013).
[21] R. Landauer, Nonlinearity: Historical and technological view, in *Nonlinearity in Condensed Matter: Proceedings of the Sixth Annual Conference, Center for Nonlinear Studies, Los Alamos, New Mexico, 1986*, edited by A. R. Bishop, D. K. Campbell, P. Kumar, and S. E. Trullinger (Springer, Berlin, 1987), pp. 2–22.
[22] M. Buttiker, J. Phys.: Condens. Matter **5**, 9361 (1993).
[23] H. Bruus and K. Flensberg, *Many-body Quantum Theory in Condensed Matter Physics—An Introduction* (Oxford University Press, Oxford, 2004).
[24] L. Brey and H. A. Fertig, Phys. Rev. B **80**, 035406 (2009).
[25] C. L. Kane and E. J. Mele, Phys. Rev. Lett. **95**, 226801 (2005).
[26] O. Shevtsov, P. Carmier, C. Petitjean, C. Groth, D. Carpentier, and X. Waintal, Phys. Rev. X **2**, 031004 (2012).
[27] H. Jiang, Z. Qiao, H. Liu, J. Shi, and Q. Niu, Phys. Rev. Lett. **109**, 116803 (2012).
[28] D. Kochan, S. Irmer, and J. Fabian, Phys. Rev. B **95**, 165415 (2017).
[29] S. Datta, *Electronic Transport in Mesoscopic Systems (Cambridge Studies in Semiconductor Physics and Microelectronic Engineering)* (Cambridge University Press, Cambridge, 1997).
[30] H. Haug and A. J. Jauho, *Quantum Kinetics in Transport and Optics of Semiconductors*, Solid-State Sciences (Springer, Berlin, 2008), Vol. 123.
[31] M. P. L. Sancho, J. M. L. Sancho, J. M. L. Sancho, and J. Rubio, J. Phys. F **15**, 851 (1985).
[32] J. Wilhelm, M. Walz, and F. Evers, Phys. Rev. B **89**, 195406 (2014).
[33] K. Wakabayashi, M. Fujita, H. Ajiki, and M. Sigrist, Phys. Rev. B **59**, 8271 (1999).
[34] L. Brey and H. A. Fertig, Phys. Rev. B **73**, 195408 (2006).